

Characterizing and modeling the efficiency limits in large-scale production of hyperpolarized ^{129}Xe

M. S. Freeman,^{1,2} K. Emami,³ and B. Driehuys^{1,2,*}¹*Center for In Vivo Microscopy, Department of Radiology, Duke University, 311 Research Drive, Durham, North Carolina 27710, USA*²*Medical Physics Graduate Program, Duke University, 2424 Erwin Road, Durham, North Carolina 27710, USA*³*Polarean, Inc., 2500 Meridian Pkwy #175, Durham, North Carolina 27713, USA*

(Received 17 February 2014; revised manuscript received 22 June 2014; published 6 August 2014)

The ability to produce liter volumes of highly-spin-polarized ^{129}Xe enables a wide range of investigations, most notably in the fields of materials science and biomedical magnetic resonance imaging. However, for nearly all polarizers built to date, both peak ^{129}Xe polarization and the rate at which it is produced fall far below those predicted by the standard model of Rb metal vapor, spin-exchange optical pumping (SEOP). In this work we comprehensively characterized a high-volume flow-through ^{129}Xe polarizer using three different SEOP cells with internal volumes of 100, 200, and 300 cm^3 and two types of optical sources: a broad-spectrum 111-W laser [full width at half maximum (FWHM) equal to 1.92 nm] and a line-narrowed 71-W laser (FWHM equal to 0.39 nm). By measuring ^{129}Xe polarization as a function of gas flow rate, we extracted the peak polarization and polarization production rate across a wide range of laser absorption levels. Peak polarization for all cells consistently remained a factor of 2–3 times lower than predicted at all absorption levels. Moreover, although production rates increased with laser absorption, they did so much more slowly than predicted by the standard theoretical model and basic spin-exchange efficiency arguments. Underperformance was most notable in the smallest optical cells. We propose that all these systematic deviations from theory can be explained by invoking the presence of paramagnetic Rb clusters within the vapor. Cluster formation within saturated alkali-metal vapors is well established and their interaction with resonant laser light was recently shown to create plasmalike conditions. Such cluster systems cause both Rb and ^{129}Xe depolarization, as well as excess photon scattering. These effects were incorporated into the SEOP model by assuming that clusters are activated in proportion to excited-state Rb number density and by further estimating physically reasonable values for the nanocluster-induced velocity-averaged spin-destruction cross section for Rb ($\langle\sigma_{\text{cluster-Rb}}v\rangle \approx 4 \times 10^{-7} \text{ cm}^3 \text{ s}^{-1}$), the ^{129}Xe relaxation cross section ($\langle\sigma_{\text{cluster-Xe}}v\rangle \approx 4 \times 10^{-13} \text{ cm}^3 \text{ s}^{-1}$), and a non-wavelength-specific photon-scattering cross section ($\sigma_{\text{cluster}} \approx 1 \times 10^{-12} \text{ cm}^2$). The resulting modified SEOP model now closely matches experimental observations.

DOI: [10.1103/PhysRevA.90.023406](https://doi.org/10.1103/PhysRevA.90.023406)

PACS number(s): 32.80.Xx, 36.40.-c, 78.67.Bf, 82.56.-b

I. INTRODUCTION

The production of hyperpolarized (HP) ^{129}Xe by spin-exchange optical pumping (SEOP) has led to many applications in scientific and medical research [1]. Polarized ^{129}Xe is used in a variety of studies such as permanent electric dipole moment searches [2], surface characterization [3], protein binding [4], biosensor development [5,6], cell spectroscopy [7], cross polarization [8], and of course biomedical magnetic resonance imaging (MRI) [9]. Particularly for clinical MRI, where scanner time is limited, HP ^{129}Xe must be generated with both high polarization and a high-production rate.

The most common approach to ^{129}Xe polarization uses spin-exchange optical pumping, wherein angular momentum is first transferred from laser photons to an alkali metal such as Rb and subsequent collisions transfer a portion of the absorbed angular momentum to the ^{129}Xe nuclei through a Fermi-contact hyperfine interaction [10]. The primary means to achieve both high polarization and a high-production rate is to employ a buffer-gas mixture lean in ^{129}Xe , flowing continuously through a Rb-filled optical pumping cell illuminated with tens to hundreds of watts of 795-nm laser light, resonant to the $D1$ absorption of Rb. Hyperpolarized ^{129}Xe is subsequently separated from the other gases by cryogenic extraction [11].

However, since large-scale continuous flow polarizers were first introduced, their performance levels, as measured by

both polarization and production rate, have fallen far short of theoretical predictions [11,12]. The first continuous-flow ^{129}Xe polarizer achieved just 2%–5% polarization in volumes of 1 L produced in 1 h while using 140 W of laser light [11]. This stood in stark contrast to predicted polarization levels of 60%–80% and production rates of 2.5 L/h.

Subsequent years saw numerous improvements that should have positively impacted polarizer performance. Initially, laser beam profiles, optics, and optical cell quality were improved so that more power illuminated the optical cell more homogeneously; however, little substantial gain was realized. Furthermore, significant improvements in laser performance, such as line narrowing the spectral profile from ~ 2 nm to ~ 0.2 nm, did not yield the advantages expected. Even greatly increased laser power [12] led to negligible improvements in both polarization and production rate. Moreover, additional phenomena were reported that could not be readily explained by standard models of SEOP. For example, polarization increased when more N_2 quenching gas was added or when lasers were detuned from the Rb $D1$ resonance [13]. Additionally, polarizers operating with richer xenon mixtures and attendant higher spin-destruction rates [13] actually exceeded in many cases the performance of polarizers using lean ^{129}Xe mixtures. Most fundamentally, perhaps the most unrecognized discrepancy has been the inability to increase the ^{129}Xe production rate by simply scaling up the laser power.

In principle, the ^{129}Xe production rate should increase as more laser light is absorbed by the alkali-metal vapor. As introduced by Bhaskar *et al.* [14], the fraction of

*bastiaan.driehuys@duke.edu

Rb- ^{129}Xe collisions resulting in spin exchange rather than alkali-metal spin destruction determines the overall efficiency with which circularly polarized photons are converted into nuclear spins. This so-called photon efficiency for ^{129}Xe -Rb spin exchange during binary collisions and short-lived molecular formation [15] was recently recalculated by Norquay *et al.* [16] to be 4.6%. That is, for every watt of 795-nm light absorbed by the ^{129}Xe -Rb system, it should be feasible to produce 25 mL/h of polarized ^{129}Xe . Hence, a polarizer absorbing 100 W of laser light should readily produce 2.5 L/h, absorbing 200 W should produce 5 L/h, and so on. In practice, however, most systems achieve nowhere near their theoretical production rate.

A significant breakthrough came with the work of Ruset *et al.* [17], who introduced a massively-scaled-up polarizer design that also greatly exceeded the performance of all compact designs described previously and since. This work introduced several design changes: (i) a vertical orientation, (ii) a large optical cell, ~ 1.8 m in length, (iii) lower-pressure operation with line-narrowed lasers, (iv) removal of bulk Rb from the cell with presaturation of the incoming gas stream with Rb vapor, (v) a cooling region prior to ^{129}Xe exiting the cell, and (vi) more gradual cryogenic accumulation. This design also touted a counterflow approach, with ^{129}Xe flowing towards the laser, although this had been a part of every flow-through ^{129}Xe production design ever published [11, 12, 18–22]. However, the improved performance was unassailable: Polarizations of 50% and production rates of 1.2 L/h were achieved.

Although the work of Ruset *et al.* represented a clear breakthrough, a fundamental explanation for the improved performance has not yet been provided [23]. Moreover, even this design did not achieve theoretical photon efficiency. A similar system to that of Ruset was thoroughly characterized by Schrank *et al.* [21], albeit with more modest 30-W laser power, and this work showed that the alkali-metal polarization was near unity, close to what was predicted by theoretical modeling. Hence, a picture began to emerge that larger polarizer designs employing optical cells with volumes of several liters and operating at relatively cooler temperatures confer a design advantage over the earlier “small and hot” designs that employ optical cells with volumes of a few hundred cm^3 , but operate at higher temperatures and alkali-metal number densities to absorb the available light. Interestingly, the recent work of Nikolaou *et al.* represents a second breakthrough [24]. They achieve very high ^{129}Xe polarization, albeit while absorbing very little of the available laser light and thus limiting production rates. Nonetheless, these demonstrations indicate that regimes exist where ^{129}Xe polarizer performance can approach theory.

This paper describes a detailed study of both ^{129}Xe polarization and production rate for a continuous-flow polarizer operating with three different cell geometries and two different laser configurations (line narrowed and free running). When these results are compared with a standard model of SEOP, it is evident that both the polarization and production rate are systematically reduced. We demonstrate that our data can be well explained if we hypothesize that vapor phase Rb does not consist only of atomic vapor but also contains nanoscale Rb clusters. Alkali metals are known to form such clusters [25] and their interaction with resonant 795-nm laser light was recently reported to create a plasmlike state [26].

Specifically, we postulate that activated clusters cause both Rb spin destruction and ^{129}Xe spin relaxation, as well as a small degree of unproductive scattering of incident laser photons. When the effects of these clusters are incorporated into the standard model, the observed polarizer performance agrees with our model to a remarkable degree.

II. THEORETICAL MODEL

A. Standard model of optical pumping

A means to model the SEOP process was introduced by Wagshul and Chupp [27] in 1989 and was recently updated by Norquay *et al.* to include the latest measured spin-exchange and spin-destruction cross sections for ^{129}Xe [16]. We use this as the standard model with two minor changes (see the Appendix). Because it was recently described in detail, we reiterate only the key elements here. Briefly, the alkali-metal polarization is calculated as a function of position z in the optical cell along the laser propagation direction according to

$$P_{\text{Rb}}(z) = \frac{\gamma_{\text{OP}}(z)}{\gamma_{\text{OP}}(z) + \Gamma_{\text{SD}}}, \quad (1)$$

where Γ_{SD} is the alkali-metal spin-destruction rate, caused by collisions of Rb with other gas species within the cell, which for binary collisions is defined by

$$\Gamma_{\text{SD}}^{\text{binary}} = \sum_i [G_i] \kappa_{\text{SD}}^{\text{Rb}-i}, \quad (2)$$

with spin-destruction coefficients $\kappa_{\text{SD}}^{\text{Rb-Rb}}$, $\kappa_{\text{SD}}^{\text{Rb-He}}$, $\kappa_{\text{SD}}^{\text{Rb-N}_2}$, and $\kappa_{\text{SD}}^{\text{Rb-Xe}}$ [15]. The optical pumping rate $\gamma_{\text{OP}}(z)$ is determined by the overlap of the frequency- and position-dependent laser intensity profile $\Phi(\nu, z)$ and the alkali-metal $D1$ absorption cross section $\sigma_s(\nu)$ according to

$$\gamma_{\text{opt}}(z) = \int_0^\infty \Phi(\nu, z) \sigma_s(\nu) d\nu. \quad (3)$$

In this one-dimensional model, photons are removed from the propagating light at each step Δz , through the optical cell, according to

$$\frac{d\Phi(\nu, z)}{dz} = -[\text{Rb}] \Phi(\nu, z) \sigma_s(\nu) [1 - P_{\text{Rb}}(z)], \quad (4)$$

where $[\text{Rb}]$ is the alkali-metal number density. The alkali-metal absorption cross section $\sigma_s(\nu)$ is taken as a Lorentzian

$$\sigma_s(\nu) = \frac{2c r_e f_{\text{osc}}}{\Gamma_{\text{FWHM}}} \frac{(\Gamma_{\text{FWHM}}/2)^2}{(\nu - \nu_0)^2 + (\Gamma_{\text{FWHM}}/2)^2}, \quad (5)$$

where c is the speed of light, r_e is the electron classical radius, and f_{osc} is the oscillator strength, which we take as 0.322 for the $D1$ transition of Rb [28]. The cross section is maximum at its resonant frequency ν_0 , while Γ_{FWHM} is the full width at half maximum of the distribution. Here Γ_{FWHM} is calculated using known pressure-broadening coefficients for Rb with the buffer gases He, Xe, and N_2 [29], which are all on the order of ~ 18 GHz/amagat. The photon flux is modeled as a roughly Gaussian function of frequency according to

$$\Phi(\nu) = \frac{P_{\text{lsr}}}{h \nu_0 A_{\text{lsr}} \delta \nu_{\text{FWHM}}} \sqrt{\frac{4 \ln 2}{\pi}} e^{-4 \ln 2 [(\nu - \nu_0)/\delta \nu_{\text{FWHM}}]^2}, \quad (6)$$

where P_{lsr} is the laser power, distributed over an area A_{lsr} , $h\nu_0$ is the photon energy, and $\delta\nu_{\text{FWHM}}$ is the full width half maximum of the laser distribution.

^{129}Xe becomes polarized by spin-exchange collisions with the polarized Rb atoms at a rate $\gamma_{\text{SE}} = \kappa_{\text{SE}}[\text{Rb}]$, where κ_{SE} is a rate constant that includes contributions from both binary collisions and pressure-dependent short-lived molecular formation [16]. We assume that ^{129}Xe interacts with a volume-averaged polarization $\langle P_{\text{Rb}} \rangle$, which is appropriate for the cell volumes and geometries considered in this paper, in which the flowing gas mixture should be highly turbulent [30]. Hence, ^{129}Xe polarization as a function of time is

$$P_{\text{Xe}}(t_{\text{res}}) = \gamma_{\text{SE}} \tau_{\text{SU}} \langle P_{\text{Rb}} \rangle (1 - e^{-t_{\text{res}}/\tau_{\text{SU}}}), \quad (7)$$

where t_{res} is the mean ^{129}Xe residence time in the optical cell and τ_{SU} is defined as

$$\frac{1}{\tau_{\text{SU}}} = \gamma_{\text{SE}} + \Gamma_1, \quad (8)$$

where Γ_1 is the ^{129}Xe -relaxation rate. For the purposes of practically characterizing the output of a flow-through polarizer, it is convenient to cast this expression in terms of the mass flow rate F through the optical cell, which is related to Xe residence time therein according to $t_{\text{res}} = V_{\text{cell}}[G]/F$, where V_{cell} is the cell volume and $[G]$ is the total gas density in the cell, in amagats. This allows us to write Eq. (7) as

$$P_{\text{Xe}}(F) = P_0(1 - e^{-F_{\text{crit}}/F}), \quad (9)$$

where F_{crit} is the critical flow rate at which Xe atoms spend, on average, one spin-up time constant τ_{SU} in the optical cell before exiting and P_0 describes the peak ^{129}Xe polarization at zero flow. This then permits us to simply define the ^{129}Xe -production rate as $F_{\text{Xe}} = f F_{\text{crit}}$, where f is the fraction of xenon in the gas mixture.

III. EXPERIMENT

A. Quantifying performance

All experiments were performed on a commercially available polarizer (Model 9800, Polarean, Inc., Durham, NC), either fitted with the standard 300-cm³ SEOP cell or retrofitted with custom-designed alternative cells with internal volumes of 100 or 200 cm³. To measure the effects of laser narrowing, two different fiber-coupled diode laser arrays were used: a broadband 111-W, 1.92-nm FWHM laser (Dual FAP, Coherent, Inc., Santa Clara, CA) and a line-narrowed 71-W, 0.39-nm FWHM laser (QPC Lasers, Laser Operations LLC, Sylmar, CA). Light from these systems was coupled via a 200-cm fiber optic to an optics box that collimated the beam, split it into horizontally and linearly polarized components, and circularly polarized each. The two beams were adjusted to maximize light transfer to the cells such that the beam that did not pass straight through the polarizing beam splitter entered the cell at a 7° angle and intersected the straight beam at the cell midpoint. We estimate that for the broad laser, 94 W of light was coupled into the cell, and for the narrowed laser, 60 W were coupled in. This 15% reduction in incident photon intensity results from reflective losses at the glass interfaces on the oven window and cell face. The measured cold cell wall relaxation times for each cell are listed in Table I.

TABLE I. Characteristics of the optical cells used in this work. Cell T_1 is measured in pure Xe at STP.

V (cm ³)	l (cm)	r (cm)	A (cm ²)	T_1 (min)
100	9.0	1.9	130	56
200	12.5	2.25	210	43
300	12.7	2.71	260	8

For each combination of laser and optical cell, ^{129}Xe polarizations vs gas-flow curves were acquired with increasing degrees of laser absorption. A gas mixture, consisting of 1% Xe (natural abundance), 10% N₂, and 89% ⁴He flowed through the optical cell at 6 atm pressure. Upon exiting the cell, the gas mixture was directed via a 150-cm length of 6.4-mm-o.d. polyurethane tubing to an ~50-cm³ test bulb housed in a volume NMR coil in the center of a polarization measurement station (Polarean, Inc., Model 2881). This system acquires ^{129}Xe NMR at 25 kHz and has sufficient sensitivity to detect ^{129}Xe polarized to 25%, within the dilute 1% mixture, with a single-shot signal-to-noise ratio of ~20. A diagram of the experimental configuration is shown in Fig. 1.

To measure polarization as a function of flow, the system was first allowed to equilibrate to the desired laser absorption level, while gas flowed slowly at 0.20 standard liter per minute [2.0-SCCM Xe (where SCCM denotes cubic centimeter per minute at STP)]. Once absorption was stable, flow was continued for a time $1.5t_{\text{res}}$ before being stopped and acquiring four ^{129}Xe NMR signals from the test bulb using a series of four 22° pulses. The $4 \times$ -averaged free-induction decays were line broadened by 0.10 Hz, Fourier transformed, and quantified by their peak height. The flow was then restarted and ^{129}Xe NMR measurements were made at successively higher flow rates in increments of 1.0 SCCM up to 10 SCCM, then 2.0 SCCM up to 20 SCCM, and then increments of 4.0 SCCM up to 36 SCCM. At each flow rate, polarization was permitted to equilibrate for $1.5t_{\text{res}}$ prior to taking ^{129}Xe -polarization measurements.

1. Converting the NMR signal to absolute polarization

To convert the signal attained within the test bulb to a quantifiable polarization, a calibration was done by simultaneously dispensing pure xenon polarized to ~10% into the bulb and a 300-cm³ Tedlar bag at atmospheric pressure. The bag was then placed on a second, calibrated measurement station to determine its absolute polarization. This station was originally calibrated against thermally polarized ¹H₂O and is recalibrated annually using a calibration transfer standard [31]. Combined with the measured signal from ^{129}Xe in the flow test station, this provided a calibration constant that required only scaling for ^{129}Xe density during polarization vs flow tests.

IV. DATA AND ANALYSIS

A. Flow curves and the standard model

Figure 2 depicts a series of representative polarization vs flow curves acquired using the line-narrowed laser illuminating a standard 300-cm³ optical cell, at 50%–100% absorption. A few trends are evident from these curves. When operating at 50% laser absorption, we observe a peak polarization of

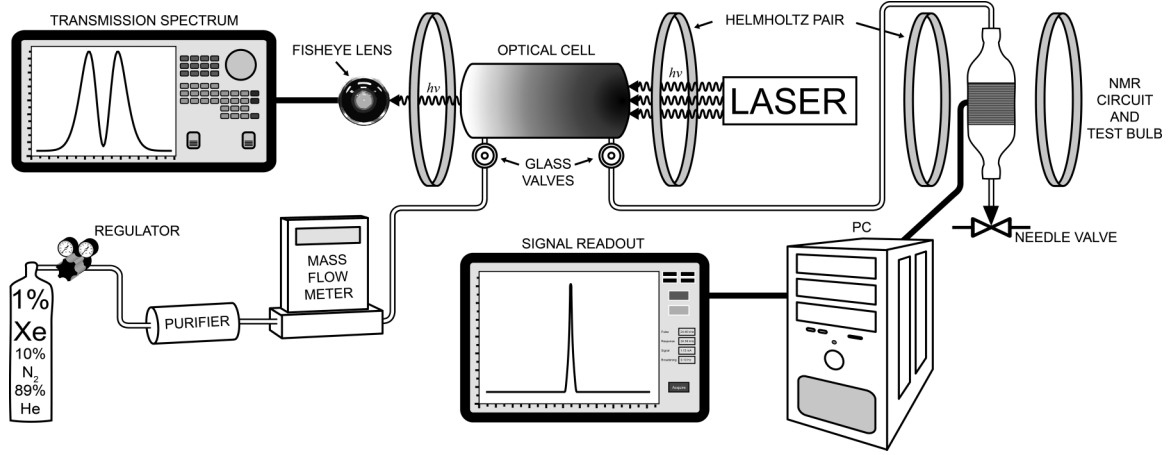


FIG. 1. Apparatus to generate polarization vs flow curves. It consists of a standard SEOP polarizer that flows directly to an adjacent NMR test bulb housed in a 20-G magnetic field where ^{129}Xe polarization is sampled by a low-frequency NMR circuit and digitized using the computer and NMR software. Laser absorption is monitored and quantified using an on-board spectrometer and photodiode. The xenon flow rate through the system is controlled by a needle valve downstream from the test bulb.

$23 \pm 2\%$ and a xenon-production rate of 12 ± 3 SCCM. As absorption increases to 80%, the peak polarization reaches a maximum of 29% before beginning to drop modestly as xenon-production rate begins to increase. For the highest 100% absorption, the peak polarization decreases to $20 \pm 6\%$, while the production rate increases to 34 ± 9 SCCM. The general trend

of increasing the production rate with increasing light absorption is qualitatively consistent with expectations from photon efficiency arguments, although the relatively low polarization and its limited variation with absorption are not consistent.

B. Comparison to the standard model

Figures 3 and 4 show plots of peak ^{129}Xe polarization and the xenon production rate fF_{crit} as a function of laser absorption for all combinations of cell geometry and laser configuration. These plots have superimposed on them the theoretically predicted polarization levels and production rates determined using the standard SEOP model. These comparisons across a range of laser absorptions illustrate a clear and systematic discrepancy between observed data and model predictions. Beginning with the 300-cm³ cell pumped with the line-narrowed laser, we note that at low absorption ^{129}Xe polarization is nearly threefold lower than predicted. This polarization gap narrows to roughly twofold at the highest absorptions. However, the xenon-production rate appears to agree very well with prediction and increases with absorption as expected.

When the same 300-cm³ cell is pumped with the broad-spectrum laser, peak ^{129}Xe polarization is nearly twofold lower than predicted at low absorption, but approaches the model at higher absorptions. The production rate for this laser-cell combination matches model predictions at low absorption, but deviates significantly below predictions at the higher-absorption levels. For the broad laser, the standard model predicts high-xenon-production rates as absorption increases because it requires absorbing the most off-resonant photons, which can only happen at very high [Rb], given the small off-resonance cross section. High [Rb] in turn would yield high-spin-exchange rates and hence high-production rates. However, such high-production rates are not seen for the broad laser, suggesting that other photon-scattering mechanisms may be coming into play.

Inspection of ^{129}Xe polarization for the smaller 200- and 100-cm³ cells shows similar discrepancies with the model

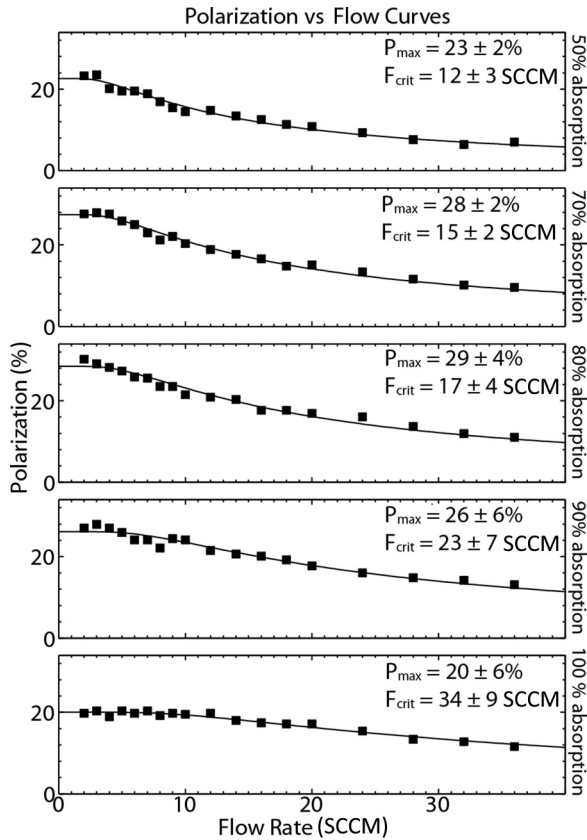


FIG. 2. Representative ^{129}Xe polarization vs flow curves acquired in the 300-cm³ cell using the line-narrowed laser at five different levels of absorption. Each of these curves can be fitted to estimate peak ^{129}Xe polarization P_0 and production rate F_{crit} .

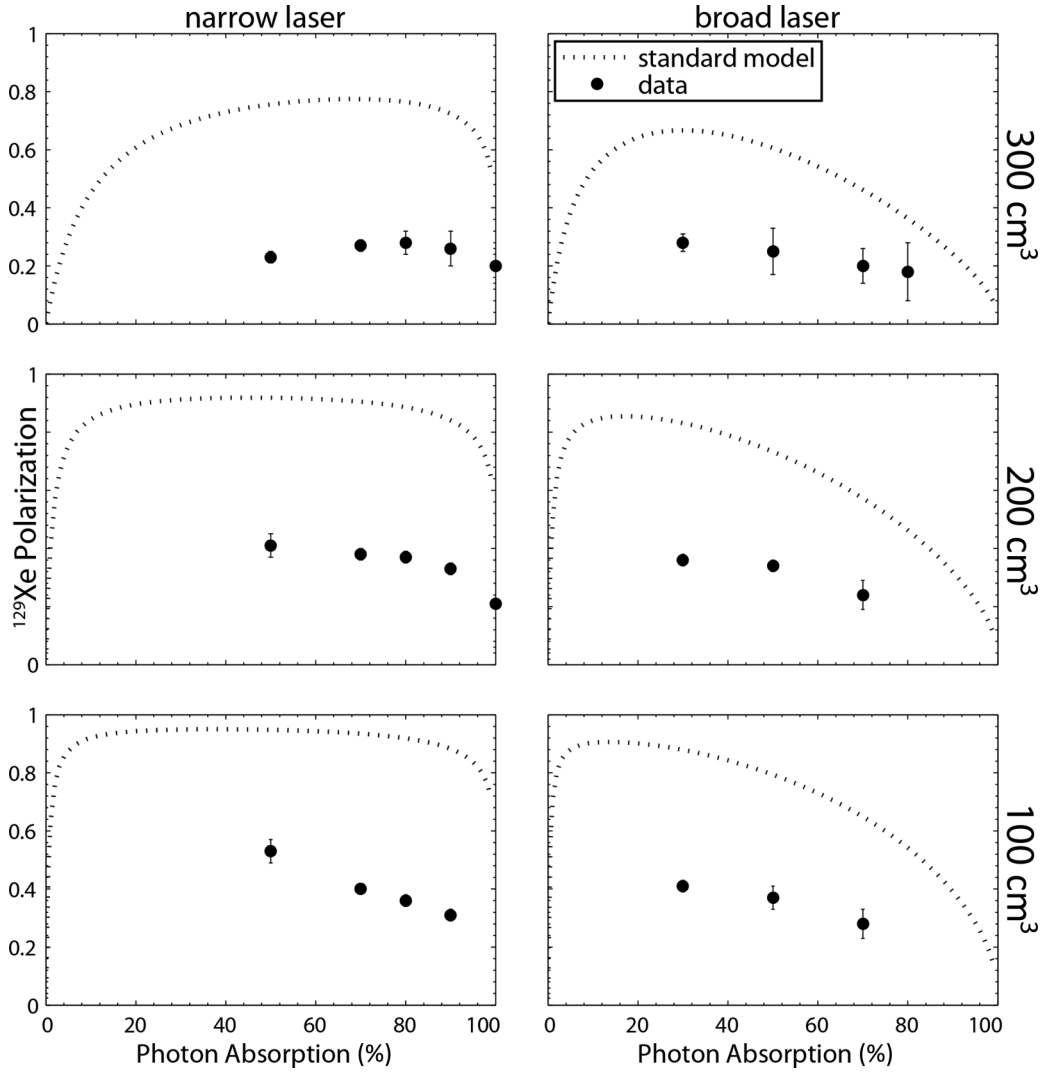


FIG. 3. Peak ^{129}Xe polarization achieved for all three cell types and pumped with both types of lasers at numerous absorption levels. Each point is the result of a single flow curve. Overlaid in the plot is the polarization predicted by the standard SEOP model.

predictions for both laser configurations. When pumping with the broad laser, ^{129}Xe polarization again starts roughly 2 \times below predictions at low absorption, with slight convergence towards model predictions at higher absorptions, although less so than seen with the 300-cm³ cell. For the narrowed laser, the ^{129}Xe -polarization discrepancy with the model is greater and remains consistently so across the range of absorption values. Observing such low ^{129}Xe polarization, even as the available laser light is being concentrated over progressively smaller areas, is suggestive of a mechanism whereby increasing laser intensity is not productively deployed to produce polarized ^{129}Xe .

An additional discrepancy between the model and measured data lies in the reduced- ^{129}Xe -production rates obtained with the smaller 200- and 100-cm³ cells. When pumping with the broad laser, the xenon-production rate is close to expectations for both cells at low absorption. However, as absorption increases, the observed production is significantly lower than model predictions. When pumping with the narrowed laser, the production rate for these smaller cells remains consistently a factor of 2 below model predictions. For example, when

absorbing 50% of narrowed light, the 200-cm³ cell produces just 12 ± 2 SCCM of HP xenon, whereas roughly twice that value is predicted. This underproduction remains roughly half the predicted values across the entire range of absorption for the narrowed laser. These findings suggest that despite concentrating the available light into smaller volume cells, the resulting absorption and/or scattering of higher-intensity laser light is not being fully converted into the production of polarized ^{129}Xe nuclei.

The diminished ^{129}Xe production achieved using smaller cells relative to larger ones is perhaps best illustrated in Fig. 5, which compares polarization vs flow curves acquired at 50% absorption of narrowed light in the 300-cm³ cell and the 100-cm³ cell. Note that the peak polarization in the smaller cell is $52 \pm 4\%$, vs $23 \pm 2\%$ in the larger cell. This result is somewhat consistent with the expectation that concentrating the available light on the half as large cell area results in 2 \times greater optical pumping rate and thus higher alkali-metal polarization. However, at such relatively low absorption, the pumping rate is not expected to limit alkali-metal polarization; the predicted volume-averaged alkali-metal polarizations in

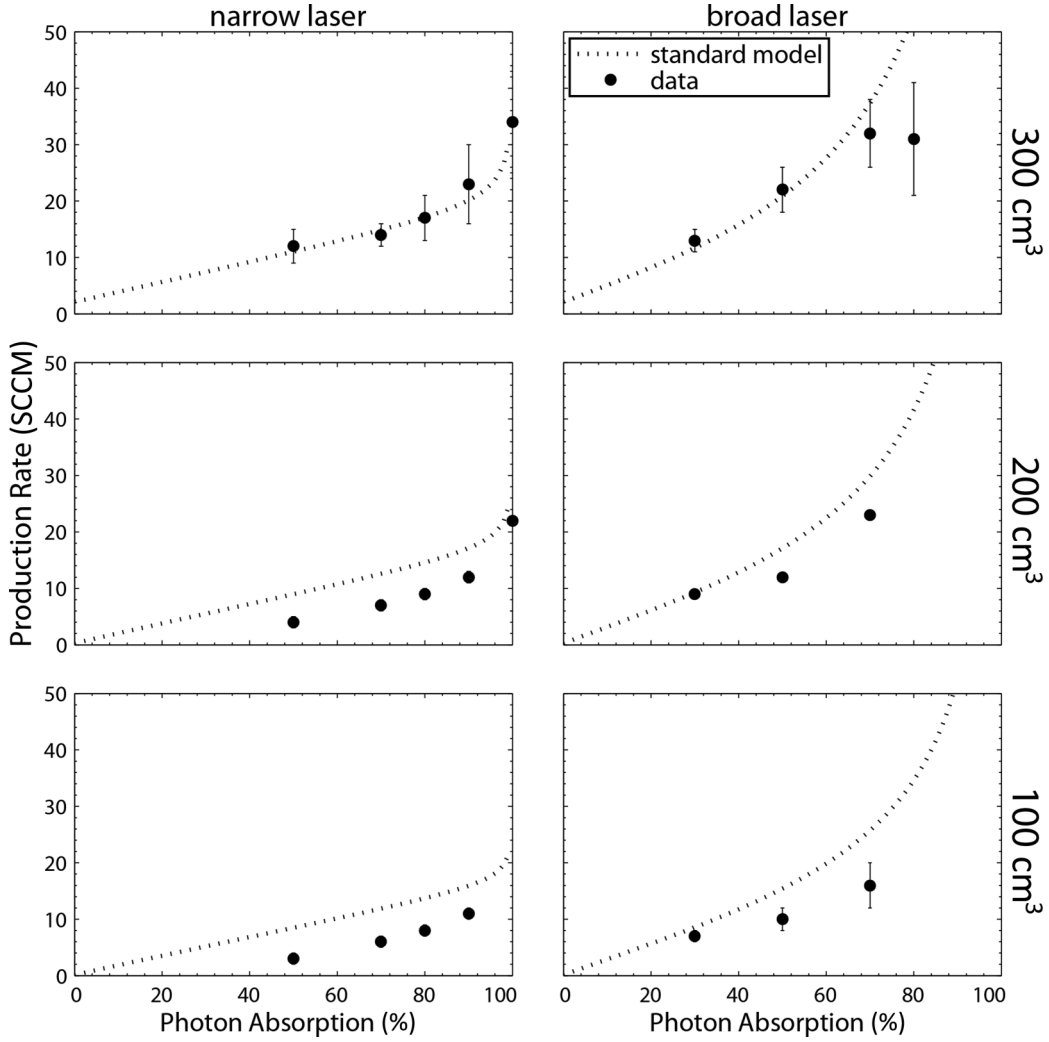


FIG. 4. Critical flow rates extracted from fitting the same flow curves as used to obtain the peak polarization depicted in Fig. 3. These values are compared to predictions of the standard SEOP model and show significant underproduction, particularly for the smaller cells and high absorption.

these cells are 91% (100-cm³ cell) and 85% (300-cm³ cell) at 50% absorption. The more striking finding is that while these cells absorb essentially the same amount of laser power (~ 30 W), the production rate is decreased in the small cell (3 ± 1 SCCM) to a quarter of that in the 300-cm³ cell (12 ± 3 SCCM). Thus, a simple geometric change that concentrates more laser light in a smaller volume and requires operating at higher alkali-metal vapor pressures to absorb that light appears to grossly reduce the photon efficiency of the system.

C. Possible extensions to the standard model of SEOP

The extensive characterization of six different cell geometry and laser combinations across a wide range of absorption conditions provides a means to evaluate and extend the standard model of ¹²⁹Xe SEOP to better account for underperformance. Thus, we seek to postulate an effect or series of effects that could augment the standard model such that the predicted performance is brought in line with our findings across all combinations of cell and laser. Such an exercise has value because it may provide insights into the mechanisms that

have lead to chronic underperformance of this and other polarizer designs. Once a model has been proposed, it is subject to testing and developing a robust means to suppress such mechanisms to regain the efficiency predicted by the standard theory. This would permit the rational design of polarizers based on fundamental insights rather than serendipitous design modifications.

To date, a large number of mechanisms have been proposed that in some way impede the efficiency of SEOP. The bulk of these mechanisms have been introduced in the context of ³He-Rb SEOP. These include (a) $P_{3/2}$ mixing and D_2 pumping [32], (b) hypothesizing a less than unity alkali-metal polarization limit [33], (c) long-range dipolar spin-exchange interactions, (d) radiation trapping [34,35], (e) energy pooling collisions [36], (f) temperature-dependent spin destruction [16], (g) imperfect circular polarization [37], or (h) skew light optical pumping [38]. Each of these effects may be playing a role, but fail to explain our range of results. Specifically, none explain the poor ¹²⁹Xe polarization at low absorption levels and its relatively unchanged nature as absorption increases. Moreover, none fully explain the utter

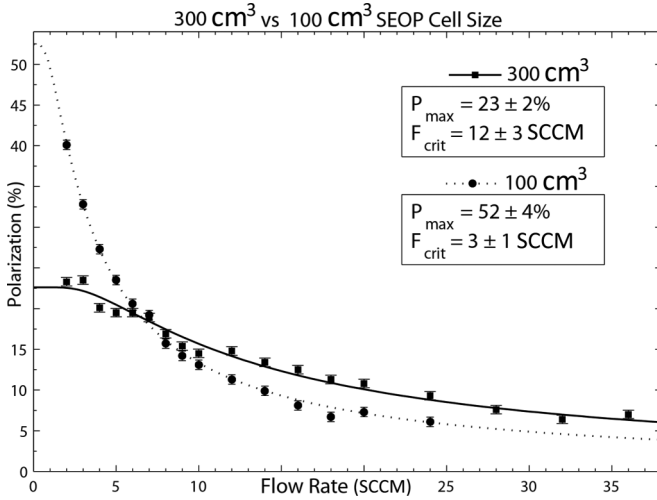


FIG. 5. Comparison of polarization vs flow curves obtained when pumping the 100- and 300- cm^3 cells with the narrowed laser, each absorbing 50% of the available light. This illustrates that although higher polarization can be achieved in the smaller cell, it comes with an unexpected fourfold penalty in production rate.

lack of benefit resulting from spectrally narrowed laser light and very poor production rates obtained when concentrating light into smaller optical cells.

Our results are also not readily explained by more pedestrian mechanisms. For example, one might consider whether poor-quality optical interfaces simply lead to far less laser power entering the cell than expected. While this could again explain poor performance at high absorption, even small amounts of laser power should still generate high ^{129}Xe polarization at low absorption, given the very dilute xenon mixture we employ; however, this is not observed. Particularly the narrowed laser, even at very low power, should generate exceedingly high alkali-metal polarization and by extension very high ^{129}Xe polarization. In fact, such high alkali-metal polarization was confirmed by Schrank *et al.* [21] in characterizing a variant of the Ruset polarizer using only 30 W. Thus, it might become tempting to explain the ^{129}Xe polarization at low absorption (low temperature) by invoking an exceedingly short ^{129}Xe wall relaxation time. However, this would require cold wall relaxation times on the order of 2 min, whereas we measured T_1 ranging from 8 to 56 min for the cells used in this study (see Table I). Moreover, even if such a short wall relaxation time were present, then ^{129}Xe polarization should increase dramatically at higher light absorption, where $[\text{Rb}]$ increases and spin-exchange rates begin to exceed wall relaxation rates. However, particularly for the narrowed-laser case, ^{129}Xe polarization is in fact almost flat across all absorptions. Thus, the mechanism responsible for suppressing ^{129}Xe polarization at low absorption appears to become steadily stronger at higher absorption such that it cannot be overcome by faster spin-exchange rates.

D. Hypothesizing laser-induced generation and activation of Rb clusters

The observations and analysis presented thus far point to the need to extend the standard SEOP model in two ways.

First, we require a mechanism that dramatically suppresses the ^{129}Xe polarization at low absorption. It must do so while still permitting high alkali-metal polarization at low absorption, as measured by Schrank *et al.* [21]. Thus, we suggest the presence of a highly paramagnetic, unpolarized species that rapidly relaxes ^{129}Xe . Moreover, to explain the lack of improvement in polarization at higher laser absorption, this mechanism must intensify with absorption. A second requirement is that it must somehow disproportionately punish the higher optical pumping efficiency of the narrowed laser relative to the broad one. However, given literature reports of exceedingly high ^{129}Xe polarization achieved in polarizers running in different regimes than we describe here, it must also be possible to remove or suppress these mechanisms through design changes. Finally, we require a mechanism that scatters off-resonance laser photons much more potently than atomic Rb. This is required to account for the remarkably efficient loss of light from the wings of the broad laser, which are depleted at far lower temperature and thus lower $[\text{Rb}]$ than predicted.

Based on these requirements, we hypothesize that the deleterious effects we observe are caused by the formation of many-atom Rb clusters. Although rarely discussed in the optical pumping literature, clusters have long been known to form in dense, supersaturated alkali-metal vapors [21]. Moreover, alkali-metal clusters have been shown to be paramagnetic, with an overall magnetic moment that increases with cluster size [39]. Of particular relevance for flow-through SEOP systems where some impurities are unavoidably introduced over time, incorporation of other atoms can enhance cluster magnetic moments [40]. In particular, incorporation of oxygen atoms into Rb clusters produces a large magnetic moment [41]. Furthermore, given their high free-electron densities, alkali-metal clusters exhibit broad (>50 nm FWHM) light scattering. Such scattering has been studied in sodium clusters and has shown to be driven by the collective resonances of the valence electrons, which exhibit a photon-absorption cross section that depends on cluster size [42].

The study of alkali-metal clusters has exploited numerous methods to deliberately promote their formation. Commonly, Rb clusters are formed by heating a Rb pool to ~ 600 K to create a high vapor pressure and then flowing a cool noble gas over it to create a supersaturated condition that causes the alkali-metal atoms to aggregate into clusters. Interestingly, Rb cluster sizes favor a distribution derived from a shell structure, which for Rb results in favored sizes with $n = 3, 9, 19, 21, 35, 41, \dots$ atoms [43]. Again, the likely introduction of O_2 impurities and reaction with atomic Rb vapor would both diminish the energy requirements for and promote formation of larger clusters at more modest temperatures [44].

Given an abundance of approaches for deliberate creation of alkali-metal clusters, it is not difficult to imagine their unintended presence in SEOP cells. However, it is somewhat more challenging to delineate an exact mechanism by which they arise and how laser light may aid their formation or activation. One possible effect of the laser is to promote light-induced atomic desorption (LIAD), wherein atomic Rb is desorbed from a surface by non-wavelength-specific light [45]. In fact, in our SEOP cells we notice that within seconds of turning on the laser, 5%–10% of the incident light is already absorbed. Although LIAD typically involves desorbing alkali

metals from polymer coated cells [46] or those containing porous silica [47], it may also occur to a modest extent in uncoated cells, especially in the presence of tens to hundreds of watts of light and macroscopic pools of Rb. Such localized increases in vapor pressure would be met in a flow-through SEOP cell, by a cool gas mixture entering the cell and creating localized supersaturation that begins the aggregation process.

The role of the laser continues once clusters have been formed. As recently shown by Atutov *et al.* [26], the incidence of 1 W cm^{-2} of $D1$ resonant light causes clusters to become unstable and explode. Atutov *et al.* observed Rb clusters exploding, fluorescing, and propagating in a solitonlike fashion through a hot buffer-gas-filled heat-pipe optical cell. Atutov *et al.* describe these exploded clusters as exhibiting a very hot plasmalike state involving significant numbers of free electrons, which would be highly depolarizing. Multiply ionized clusters have temperatures approaching their boiling point and atoms within the cluster behave like a liquid [48]. Beyond this point, as clusters ionize further, their internal energy causes them to explode. It is particularly noteworthy that Atutov *et al.* noticed that incident light had to be within 5 GHz of the $D1$ resonance to cause clusters to fragment.

The emerging picture of cluster formation and destruction by laser light may also play a role in the commonly observed phenomenon of rubidium runaway in ^{129}Xe SEOP systems [49,50]. The formation of Rb clusters would likely be concentrated near high-intensity laser irradiation of alkali-metal atoms near bulk alkali-metal pools on the optical cell surface. The LIAD effect creates localized high vapor pressure, which when combined with the flow of cool gas or convection creates a supersaturated vapor that promotes particle agglomeration. Subsequent irradiation of clusters by resonant $D1$ light causes cluster explosion into vapor, with increased heating, and further supersaturation. Thus, one can conceive of a rapid and dynamic cycle wherein clusters are formed, absorb energy, release electrons into a plasmalike state, and energetically explode. Alkali-metal vapor and fragments are eventually incorporated into new clusters and are convectively dispersed throughout the vapor in the SEOP cell.

1. Modeling Rb clusters

With this background in mind, we seek to model the clusters in the simplest possible way until such a time that they may be better characterized. To simplify the complex dynamic state of clusters and calculate their effects on polarization, we refer to them at any point within their formation and destruction cycle as activated clusters. Such clusters would have several effects. First, the presence of these large paramagnetic clusters and related plasmas must relax ^{129}Xe nuclei. We model this process simply as collisional relaxation between ^{129}Xe and the cluster according to

$$\frac{1}{T_{1\text{Xe}}} = [\text{Rb}_n^{z+}] \langle \sigma_{\text{cluster-Xe}} v \rangle, \quad (10)$$

where $[\text{Rb}_n^{z+}]$ is the activated cluster number density, in which n signifies the unknown, but non-negligible, number of atoms in the cluster and $z+$ signifies its unknown, but non-negligible, ionization state. Further, akin to spin-exchange formalism, $\langle \sigma_{\text{cluster-Xe}} v \rangle$ is the velocity-averaged relaxation cross section

for ^{129}Xe -cluster collisions. Given their large size, Rb_n^{z+} clusters should exhibit a much larger collisional cross section with ^{129}Xe than would their atomic Rb counterparts. Estimates of Rb cluster size from the literature range from $\sim 40 \text{ nm}$ when formed at very low buffer-gas pressure [51] to $\sim 600 \text{ nm}$ when formed at higher pressure and irradiated with $\sim 1 \text{ W cm}^{-2}$ of $D1$ resonant light [26]. With these geometrical considerations in mind, we estimate the cross section for ^{129}Xe atoms colliding with Rb clusters to be 4–6 orders of magnitude larger than for atomic Rb. Assuming a less efficient spin interaction than for atomic Rb- ^{129}Xe and through further steepest-descent tuning detailed below, we arrive at an estimated velocity-averaged cross section of $\langle \sigma_{\text{clusters-Xe}} v \rangle \approx 4 \times 10^{-13} \text{ cm}^3 \text{ s}^{-1}$. This is roughly 3 orders of magnitude larger than the measured Rb- ^{129}Xe velocity-averaged spin-exchange cross section. Thus, even a small number density of clusters could begin to compete with spin exchange to suppress ^{129}Xe polarization.

If activated Rb clusters have a relaxing effect on ^{129}Xe , they must also cause Rb spin destruction. We characterize this spin destruction using the same standard collisional formalism

$$\Gamma_{\text{SDclusters}} = [\text{Rb}_n^{z+}] \langle \sigma_{\text{cluster-Rb}} v \rangle, \quad (11)$$

where $\langle \sigma_{\text{cluster-Rb}} v \rangle$ is the velocity-averaged Rb relaxation cross section induced by cluster collisions. Through similar estimates as outlined above we estimate this cross section to be $\langle \sigma_{\text{cluster-Rb}} v \rangle \approx 4 \times 10^{-7} \text{ cm}^3 \text{ s}^{-1}$. By comparison, the atomic Rb-Rb spin-destruction cross section is $\langle \sigma_{\text{Rb-Rb}} v \rangle = 4.2 \times 10^{-13} \text{ cm}^3 \text{ s}^{-1}$ [52]. Again, the relatively larger size of clusters would endow them with comparatively enormous collisional cross sections relative to pure atom-atom interactions.

Finally, we model the broadband scattering of laser photons by clusters by endowing them with a wavelength-independent scattering cross section that wastes photons in proportion to their density $[\text{Rb}_n^{z+}]$. Again using the steepest-descent optimization described below, we estimate this scattering cross section to be

$$\sigma_{\text{cluster}} \approx 1 \times 10^{-12} \text{ cm}^2, \quad (12)$$

which is roughly an order of magnitude larger than the peak scattering cross section for the atomic Rb $D1$ resonance under the conditions in our cell. This estimate substitutes for what is likely to be an overlap of many Mie-scattering profiles arising from a broad distribution of cluster sizes.

With the physical effects of activated clusters included in the model, the remaining task is to postulate a means of scaling their number density. We seek to account for two factors that we have empirically observed to diminish polarizer performance. The first is that neither polarization nor production rate improve when laser intensity increases or spectral width is narrowed. Second, higher alkali-metal vapor pressure in smaller cells appears to negatively impact performance. For these reasons, we model cluster density as being proportional to the excited-state Rb population. This incorporates increased optical pumping rate (through either narrowing or concentrating laser light), increased spin-destruction rates, and higher alkali-metal vapor pressure into the cluster generation mechanism. Note that this approach has been empirically found to best explain our measurements. We also attempted to scale cluster number density according to

Rb number density alone, optical pumping rate alone, gas temperature, and photon intensity. None of these approaches agreed with observation to the same extent. The excited-state Rb density is given by

$$[\text{Rb}_{5p+1/2}] = \tau \gamma_{\text{OP}} [\text{Rb}] (1 - P_{\text{Rb}}), \quad (13)$$

where τ is the excited-state lifetime. Substituting for P_{Rb} as defined in Eq. (1) into Eq. (13) and subsuming the lifetime into the overall scaling constant Θ_{cluster} , we obtain an expression for cluster density as a function of alkali-metal density of

$$[\text{Rb}_n^{z+}] = \Theta_{\text{cluster}} \left(\frac{\gamma_{\text{OP}} \Gamma_{\text{SD}}}{\gamma_{\text{OP}} + \Gamma_{\text{SD}}} \right) [\text{Rb}]. \quad (14)$$

This way of modeling cluster number density $[\text{Rb}_n^{z+}]$ thus increases as a function of $[\text{Rb}]$, as well as γ_{OP} and Γ_{SD} . This approach appears to appropriately punish operating at higher alkali-metal number density, as well as penalizing high optical pumping rates achieved by laser narrowing or concentrating power in a smaller volume. We should note, however, that the overall scaling of activated cluster number density and the postulated cross sections are not fully independent. Thus, the

same modeling effect can be achieved by increasing cluster density and decreasing the associated cross sections or vice versa. Thus, as a starting point for the model we have set the overall scale such that $[\text{Rb}_n^{z+}]$ is roughly 1/1000 the number density of atomic Rb at 100 °C. This gives us a starting constant $\Theta_{\text{cluster}} = 6.5 \times 10^{-8}$ s.

E. Steepest-descent tuning of cluster parameters

To arrive at the best possible estimates of the associated cross sections and number density scaling, we wish to fit the entirety of our collected data set. However, since these data do not have a simple analytical function, an alternative approach is to use a steepest-descent gradient fitting routine to minimize least-squares differences with the model results. We allowed only three model parameters to be adjusted: $\langle \sigma_{\text{cluster-Rb} \nu} \rangle$, $\langle \sigma_{\text{cluster-Xe} \nu} \rangle$, and σ_{cluster} . These same parameters were used to collectively fit the entire data set, including polarization and production rate at all absorption levels, for all six combinations of cell geometry and laser configuration. Prior to running the steepest-descent gradient algorithm, a baseline starting guess

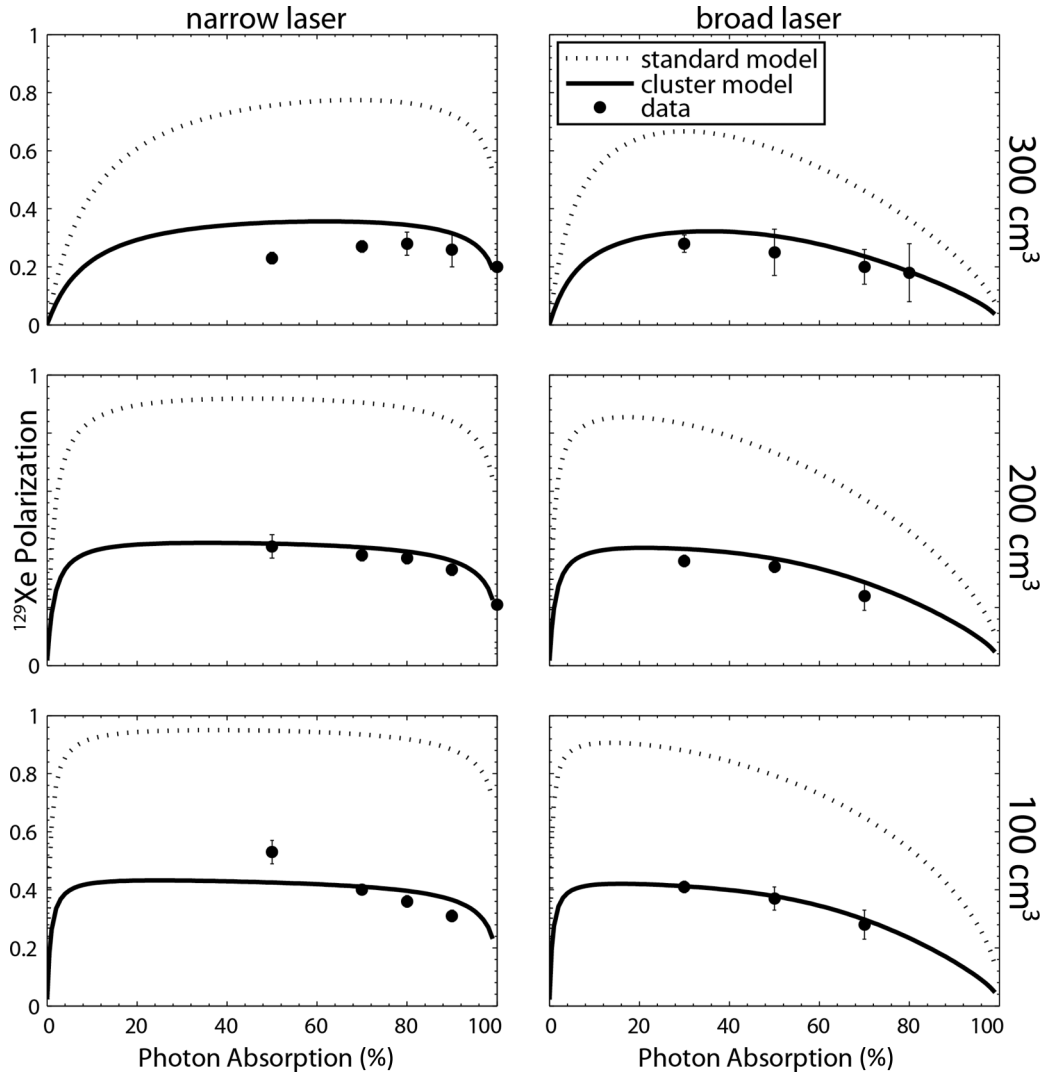


FIG. 6. ^{129}Xe peak polarization data from Fig. 3, but now including predictions of the cluster model (bold curve) showing significantly better agreement than the standard SEOP model (dotted curve).

for all the parameters was adjusted until the predictions of the model came into good visual agreement with the data. Then a random number generator varied all six values between $0\times$ and $2\times$ the values found in the qualitative fit 51 751 times. The best fit from that sequence was then run through a steepest-descent gradient fitting routine to further optimize the parameters toward a global minimum. The technique used a cost function consisting of a least-squares difference between the 24 polarization data points and the numerical model, as well as the differences for the 24 production rate data points and the model.

F. Results of steepest-descent modeling

The results of the steepest-descent fits appear in Fig. 6 showing peak polarization data compared to the optimized model and Fig. 7 showing the production rate compared to the optimized model. Note that peak polarization now agrees well across the entire range of absorptions for all six combinations of laser and optical cell geometry. In particular, the low-absorption polarization, which so greatly underperforms the standard model, is now pulled into line

TABLE II. Proposed cluster scaling constant, cluster relaxation cross sections, and scattering cross section determined from the steepest-descent fit.

Θ_{cluster}	$\langle\sigma_{\text{cluster-Rb}v}\rangle$	$\langle\sigma_{\text{cluster-Xe}v}\rangle$	σ_{cluster}
$6.5 \times 10^{-8} \text{ s}$	$4 \times 10^{-7} \text{ cm}^3 \text{ s}^{-1}$	$4 \times 10^{-13} \text{ cm}^3 \text{ s}^{-1}$	$1 \times 10^{-12} \text{ cm}^2$

by cluster-induced relaxation of the ^{129}Xe . This mechanism of polarization suppression continues to grow towards higher absorption levels. The model also appears to better predict the observed production rates (Fig. 7). For the narrowed laser, the model correctly predicts the poorer photon efficiency for the smaller optical cells. For the broad laser, the model now does a good job of slowing the predicted production rates at higher absorption levels. The hypothetical cluster cross sections used to generate these curves are listed in Table II.

G. Comparison of individual cluster effects

The present activated-cluster model comes into agreement with the data through the addition of three cluster-initiated

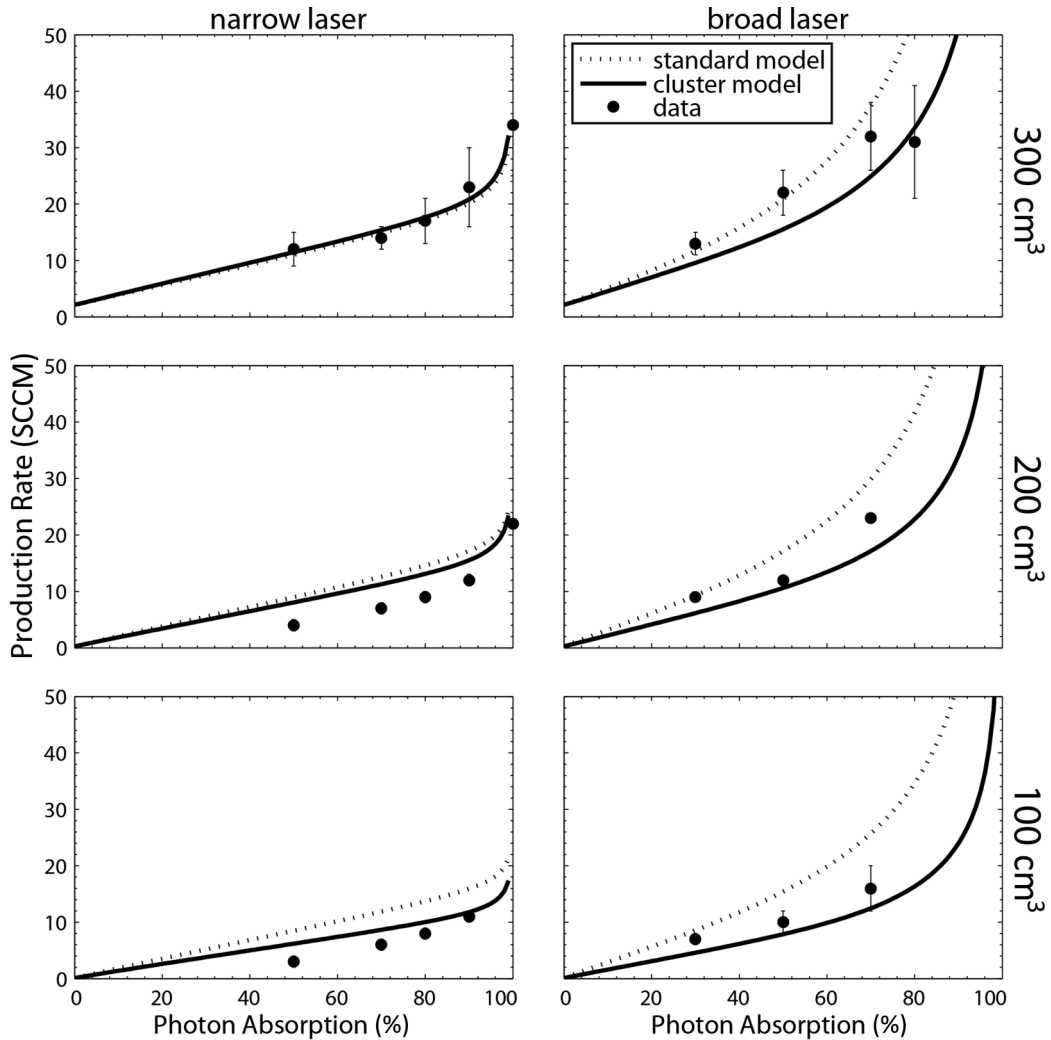


FIG. 7. ^{129}Xe production rates from Fig. 4, now compared to the cluster model (bold curve), which shows considerably better agreement across absorption levels than the standard model (dotted curve).

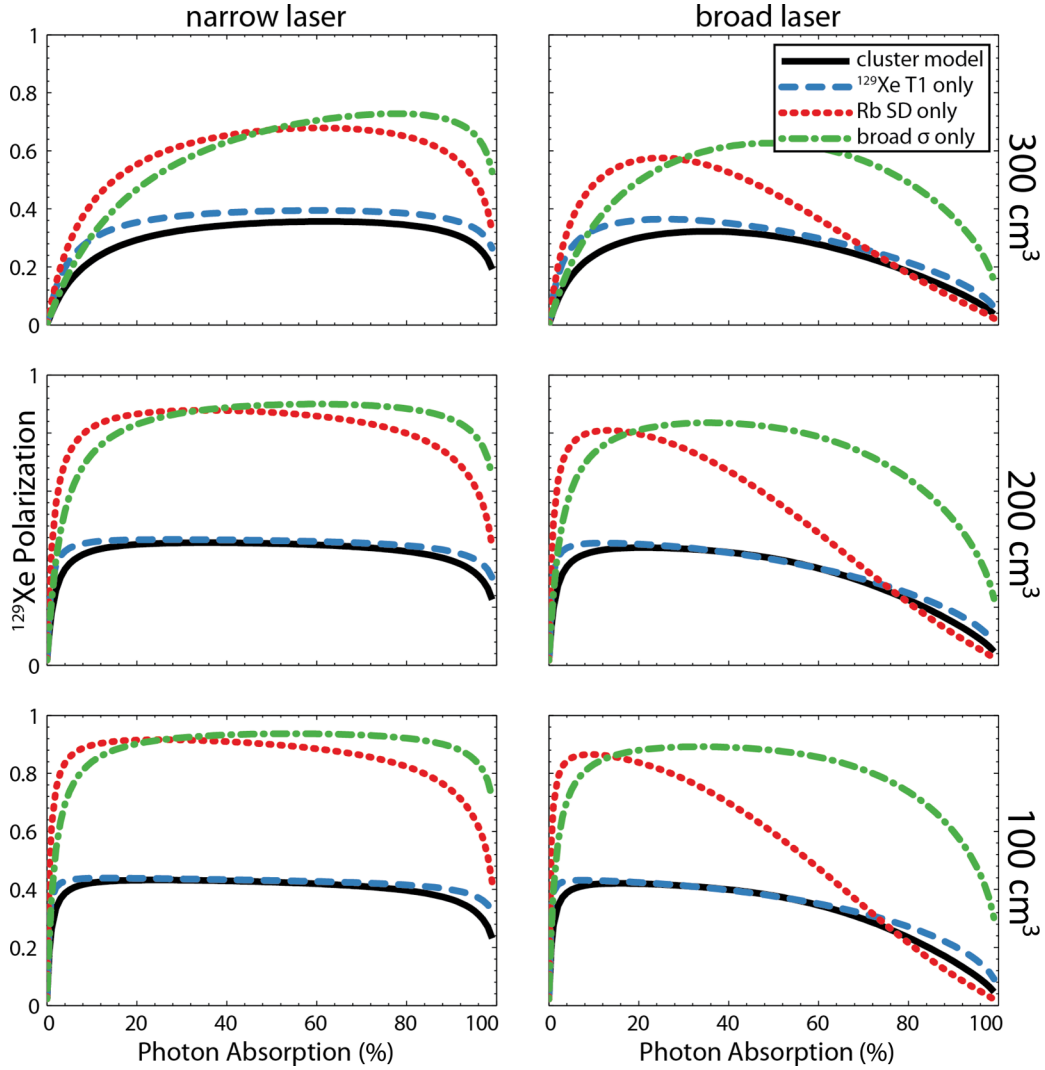


FIG. 8. (Color online) ^{129}Xe peak polarization data from the cluster model in Fig. 6 (black curve), but now including predictions of the individual effects of the model, that is, the standard model with only the addition of the ^{129}Xe T_1 relaxation effect (blue curve), the Rb spin-destruction effect (red curve), and broad photon absorption effect (green curve).

effects, a velocity-averaged spin-destruction cross section $\langle\sigma_{\text{cluster-Rb}}v\rangle$, a velocity-averaged ^{129}Xe relaxation cross section $\langle\sigma_{\text{cluster-Xe}}v\rangle$, and a broad photon-absorption cross section σ_{cluster} . To appreciate the individual influence of each of these mechanisms, their effect on predicted polarization and production rate are shown in Figs. 8 and 9. For these figures the standard model was run, while adding in only one additional effect at a time (the red curve is for spin destruction, green for light scattering, and blue for ^{129}Xe relaxation), and compared against the full cluster model (black curve).

1. Spin destruction

When only the effect of cluster-induced spin destruction on the atomic Rb is added to the standard model (shown in red in Figs. 8 and 9), it effectively reduces ^{129}Xe polarization at higher laser absorption levels, but has relatively little effect at the lower absorption levels. Hence, alkali-metal polarization can remain high at low absorption levels, consistent with the findings of Schrank *et al.* [21]. Cluster-induced alkali-metal spin destruction at high absorption has a more deleterious

effect on ^{129}Xe polarization for the broad laser than the narrowed laser. That is because high absorption occurs at higher [Rb] for the broad laser and clusters grow in proportion to [Rb].

Regarding production rate, the cluster-induced spin destruction again has little impact at low absorption on any cell configuration. However, as absorption increases, increased alkali-metal spin destruction suppresses production rate more significantly for the narrowed laser than for the broad laser. The narrowed laser, with its higher optical pumping rate, creates a higher cluster number density. This in turn results in a larger fraction of atomic Rb relaxation coming from collisions other than ^{129}Xe -Rb spin-exchange collisions. Thus, cluster-induced spin Rb destruction undermines photon efficiency.

2. Broad photon scattering

The effect of cluster-related photon scattering (green curve) on ^{129}Xe polarization is somewhat similar to that of Rb spin destruction. It again does not significantly suppress ^{129}Xe

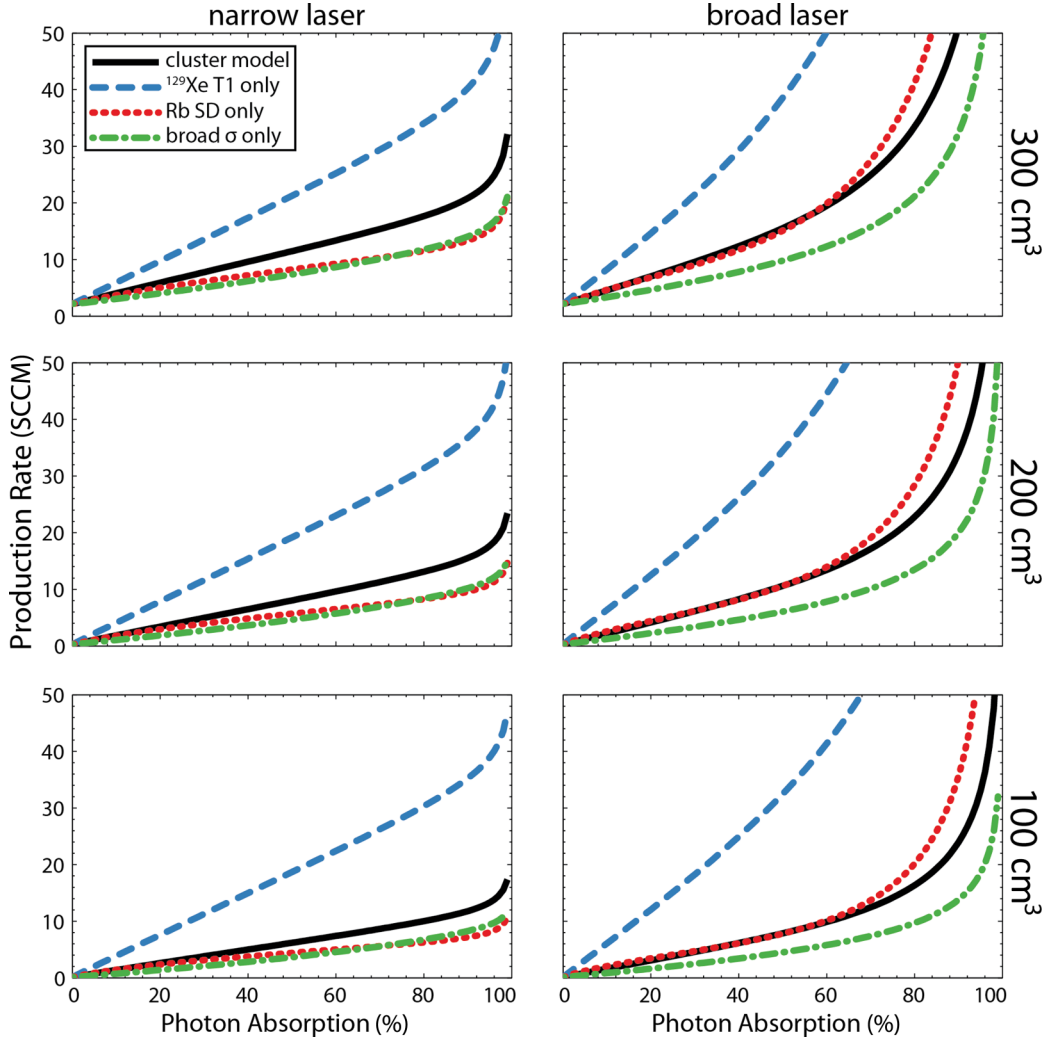


FIG. 9. (Color online) ^{129}Xe production rates from Fig. 7, but now including predictions of the individual effects of the model, ^{129}Xe T_1 relaxation (blue curve), Rb spin-destruction (red curve), and broad photon absorption (green curve) as compared to the full cluster model (black curve).

polarization at low absorption, but has its most substantial impact at the higher absorption levels. It has the primary effect of decreasing production rates across the board, as laser photons are being unproductively scattered rather than pumping atomic Rb. In fact, for all cell and laser combinations, this effect actually suppresses production rate *below* the rate seen in the final model. That is because in the final model the production rate is actually artificially enhanced partially by exceedingly short ^{129}Xe T_1 , discussed in the next section. The photon-scattering term was necessary to enable predicting *both* ^{129}Xe polarization and production rate for all combinations of cell and laser.

3. ^{129}Xe relaxation

Cluster-induced ^{129}Xe spin relaxation (blue line) actually appears to provide the bulk of the polarization-limiting effects. For the example of the 100-cm³ SEOP cell pumped by the broad laser, the ^{129}Xe relaxation time T_1 caused by clusters at only 10% absorption is 2 min. By the time 90% absorption is reached the ^{129}Xe T_1 has been reduced to only

8 s. As mentioned, this short ^{129}Xe T_1 actually artificially increases apparent production rates, much like the way in which ^3He cells with very poor wall relaxation times actually exhibit accelerated spin-up times. In this case, the artificially accelerated production rates are somewhat counterbalanced by the even slower than predicted production rates from true atomic Rb- ^{129}Xe spin exchange.

H. Possible presence of activated clusters in ^3He cells

Although the work presented here is focused entirely on ^{129}Xe polarization, it is tempting to consider the possibility that clusters may also play a role in ^3He SEOP. Although ^3He polarization is typically quite high, it remains plagued by an X factor [53,54], which behaves somewhat like a temperature-dependent wall relaxation rate that causes cell-to-cell performance variations and scales loosely with their surface-to-volume ratio. Moreover, although impressive ^3He polarization levels exceeding 80% are now routinely attained [55], these systems still consume considerably more laser light than should be necessary. Such observations could

potentially also be attributable to cluster formation. For example, cluster-induced relaxation of ^3He could be difficult to distinguish from enhanced wall relaxation and clusters could also be responsible for excessive scattering of laser light. However, as we have modeled their formation, cluster generation should be considerably weaker in ^3He cells than ^{129}Xe cells. This is because alkali-metal spin destruction in ^3He cells is orders of magnitude lower than in ^{129}Xe cells. Thus, excited-state Rb density should be considerably lower in ^3He cells and cluster number density, as estimated by Eq. (14), would be reduced. Moreover, ^3He SEOP does not involve flow. It takes place in an ultrapure environment with uniform temperature, which reduces the conditions of alkali-metal supersaturation that are promoted by cool gas flowing into a hot cell. The absence of flow also diminishes the introduction of contaminants such as O_2 and H_2O . Without such contaminants, cluster formation is likely inhibited and cluster size is likely reduced [44]. Nonetheless, the arguments presented here certainly suggest that the Rb cluster formation could be occurring in ^3He SEOP as well.

V. DISCUSSION AND CONCLUSION

A large body of literature describing high-volume production of hyperpolarized ^{129}Xe and ^3He indicates that the standard model of SEOP is missing a key component needed to explain observed performance. By postulating the generation of spin-destroying, ^{129}Xe relaxing, broadly absorbing Rb clusters and including their effects in the model, we are now able to retroactively predict the performance of our existing polarizers under a large variety of conditions. Although the possibility of generating such clusters is bolstered by the observations of Atutov *et al.* [26] and several decades of alkali-metal cluster literature, it is important to note that we have not yet taken steps to confirm their presence in our SEOP system or any other. However, this relatively simple and physically plausible mechanism does a remarkably good job of explaining observed performance, not just at a single operating point, but across a wide range of laser absorption and a wide range of cell and laser combinations.

Of course, we should note that even if Rb cluster formation is confirmed, the proposed model of their formation and effects on ^{129}Xe relaxation, Rb spin destruction, and optical scattering will undoubtedly be found to be overly simplistic and the resulting cross sections only crude approximations. In fact, it is unlikely that such clusters would even form with a uniform size, but instead would likely exhibit a distribution of sizes. However, it stands to reason that some aspects of these three behaviors will be found to persist and their effects will manifest themselves at least qualitatively as postulated here.

One approach to aid in the search for clusters would be to exploit their nonresonant scattering properties. For example, a cell during optical pumping could be interrogated with a broad-spectrum white-light source delivered transverse to the optical pumping direction. The resulting extinction spectra may show characteristic Mie scattering from clusters and perhaps enable reporting on approximate cluster size [51]. Alternatively, fluorescence spectra reflecting emission of photons from deexcitation of clusters or fragments could represent a second approach to their detection [36].

It is clear that if methods can be developed to directly detect the presence of Rb clusters, their systematic elimination from SEOP systems should be possible. In fact, the recently published results of Nikolaou *et al.* [24] already provide encouragement that this can be achieved. This polarizer, operating at very low temperatures and number densities compared to continuous flow polarizers, appears to be one of the few with ^{129}Xe polarization that is entirely in line with the predictions of the standard model. This provides encouragement that elimination of clusters from large-scale polarized ^{129}Xe production will result in the ability to routinely and cost-effectively build ^{129}Xe polarization systems that produce liters of polarized ^{129}Xe on demand at polarizations exceeding 50%.

ACKNOWLEDGMENTS

This study was funded by the NIH, NHLBI (Grant No. R01 HL105643) and NCI Grant No. R01 CA142842. The work was performed at the Duke Center for In Vivo Microscopy, an NIH, NIBIB National Biomedical Technology Resource Center (through Grant No. P41 EB015897). The authors thank Zackary Cleveland for helpful discussions and Sally Zimney for carefully reading the manuscript.

APPENDIX: MODIFICATIONS TO THE STANDARD MODEL AS REPORTED BY NORQUAY *ET AL.*

The basic premise of the standard model used in this work is identical to that outlined by Norquay *et al.* [16]. However, we have made two modifications with regard to calculating Rb spin destruction and the effects of van der Waals molecules. First, we found it necessary to change the way in which the temperature dependence of three of the binary spin-destruction coefficients ($\kappa_{\text{SD}}^{\text{Rb-He}}$, $\kappa_{\text{SD}}^{\text{Rb-N}_2}$, and $\kappa_{\text{SD}}^{\text{Rb-Xe}}$) is used to calculate the binary spin-destruction rate as defined by Eq. (2). While their spin-destruction coefficients for He and N_2 scale with absolute temperature (in degrees Kelvin), as is customary, they scale Xe-Rb spin destruction in degrees Celsius. This may have been an error because it would imply zero spin destruction at 0°C and negative spin destruction below that temperature.

Thus, we adopt the commonly used method of scaling with $(T/298\text{ K})^X$. Using the most recent literature values, we use the temperature-dependent spin-destruction coefficients of $\kappa_{\text{SD}}^{\text{Rb-He}} = 3.45 \times 10^{-19} (T/298\text{ K})^{4.26} \text{ cm}^3 \text{ s}^{-1}$ [52], $\kappa_{\text{SD}}^{\text{Rb-N}_2} = 3.44 \times 10^{-18} (T/298\text{ K})^3 \text{ cm}^3 \text{ s}^{-1}$ [56], and $\kappa_{\text{SD}}^{\text{Rb-Xe}} = 6.02 \times 10^{-15} (T/298\text{ K})^{1.17} \text{ cm}^3 \text{ s}^{-1}$ [15]. Note that this form has the added benefit that the coefficients preceding the temperature term represent the room-temperature value of the parameter of interest and thus provides some intuitive value. Moreover, for an abundance of clarity, we express the equation for spin exchange induced by van der Waals molecules introduced by Norquay *et al.* [57] in the format

$$\gamma_{\text{SE}}^{\text{vdW}} = \frac{[\text{Rb}]}{\sum_i ([G_i]/\xi_i)} \quad (\text{A1})$$

and use the values for ξ , the van der Waals-specific rates, for He, N_2 , and Xe as reported by Norquay *et al.*

- [1] B. M. Goodson, *J. Magn. Reson.* **155**, 157 (2002).
- [2] M. V. Romalis and M. P. Ledbetter, *Phys. Rev. Lett.* **87**, 067601 (2001).
- [3] M.-A. Springuel-Huet, J.-L. Bonardet, A. Gédéon, and J. Fraissard, *Magn. Reson. Chem.* **37**, S1 (1999).
- [4] L. Schröder, T. J. Lowery, C. Hilty, D. E. Wemmer, and A. Pines, *Science* **314**, 446 (2006).
- [5] M. M. Spence, S. M. Rubin, I. E. Dimitrov, E. J. Ruiz, D. E. Wemmer, A. Pines, S. Q. Yao, F. Tian, and P. G. Schultz, *Proc. Natl. Acad. Sci. USA* **98**, 10654 (2001).
- [6] T. J. Lowery, S. M. Rubin, E. J. Ruiz, M. M. Spence, N. Winssinger, P. G. Schultz, A. Pines, and D. E. Wemmer, *Magn. Reson. Imaging* **21**, 1235 (2003).
- [7] J. Wolber, A. Cherubini, M. O. Leach, and A. Bifone, *Magn. Reson. Med.* **43**, 491 (2000).
- [8] G. Navon, Y. Q. Song, T. Rõm, S. Appelt, R. E. Taylor, and A. Pines, *Science* **271**, 1848 (1996).
- [9] B. Driehuys, G. P. Cofer, J. Pollaro, J. Boslego, L. W. Hedlund, and G. A. Johnson, *Proc. Natl. Acad. Sci. USA* **103**, 18278 (2006).
- [10] T. G. Walker and W. Happer, *Rev. Mod. Phys.* **69**, 629 (1997).
- [11] B. Driehuys, G. Cates, E. Miron, K. Sauer, D. Walter, and W. Happer, *Appl. Phys. Lett.* **69**, 1668 (1996).
- [12] A. L. Zook, B. B. Adhyaru, and C. R. Bowers, *J. Magn. Reson.* **159**, 175 (2002).
- [13] P. Nikolaou, N. Whiting, N. A. Eschmann, K. E. Chaffee, B. M. Goodson, and M. J. Barlow, *J. Magn. Reson.* **197**, 249 (2009).
- [14] N. D. Bhaskar, W. Happer, and T. McClelland, *Phys. Rev. Lett.* **49**, 25 (1982).
- [15] I. A. Nelson and T. G. Walker, *Phys. Rev. A* **65**, 012712 (2001).
- [16] G. Norquay, S. R. Parnell, X. Xu, J. Parra-Robles, and J. M. Wild, *J. Appl. Phys.* **113**, 044908 (2013).
- [17] I. C. Ruset, S. Ketel, and F. W. Hersman, *Phys. Rev. Lett.* **96**, 053002 (2006).
- [18] H. Imai, J. Fukutomi, A. Kimura, and H. Fujiwara, *Concept Magn. Reson.* **33B**, 192 (2008).
- [19] S. E. Korchak, W. Kilian, and L. Mitschang, *Appl. Magn. Reson.* **44**, 65 (2013).
- [20] M. Rosen, T. Chupp, K. Coulter, R. Welsh, and S. Swanson, *Rev. Sci. Instrum.* **70**, 1546 (1999).
- [21] G. Schrank, Z. Ma, A. Schoeck, and B. Saam, *Phys. Rev. A* **80**, 063424 (2009).
- [22] D. K. Walter, W. M. Griffith, and W. Happer, *Phys. Rev. Lett.* **86**, 3264 (2001).
- [23] F. W. Hersman *et al.*, *Acad. Radiol.* **15**, 683 (2008).
- [24] P. Nikolaou *et al.*, *Proc. Natl. Acad. Sci. USA* **110**, 14150 (2013).
- [25] D. Mann and H. Broida, *J. Appl. Phys.* **44**, 4950 (1973).
- [26] S. Atutov, A. Plekhanov, A. Shalagin, R. Calabrese, L. Tomassetti, and V. Guidi, *Eur. Phys. J. D* **66**, 140 (2012).
- [27] M. E. Wagshul and T. E. Chupp, *Phys. Rev. A* **40**, 4447 (1989).
- [28] G. Drake, *Atomic, Molecular and Optical Physics Handbook* (AIP, New York, 1996).
- [29] M. V. Romalis, E. Miron, and G. D. Cates, *Phys. Rev. A* **56**, 4569 (1997).
- [30] A. Fink and E. Brunner, *Appl. Phys. B* **89**, 65 (2007).
- [31] I. Nelson, B. Driehuys, and S. Kadlecsek, Proceedings of the 12th Annual Scientific Meeting of the ISMRM, Kyoto, 2004 (unpublished), p. 1689.
- [32] L. Krause, *Appl. Opt.* **5**, 1375 (1966).
- [33] E. Babcock, I. Nelson, S. Kadlecsek, B. Driehuys, L. W. Anderson, F. W. Hersman, and T. G. Walker, *Phys. Rev. Lett.* **91**, 123003 (2003).
- [34] M. E. Wagshul and T. E. Chupp, *Phys. Rev. A* **49**, 3854 (1994).
- [35] M. A. Rosenberry, J. P. Reyes, D. Tupa, and T. J. Gay, *Phys. Rev. A* **75**, 023401 (2007).
- [36] I. Saha, P. Nikolaou, N. Whiting, and B. M. Goodson, *Chem. Phys. Lett.* **428**, 268 (2006).
- [37] B. Lancor, E. Babcock, R. Wyllie, and T. G. Walker, *Phys. Rev. A* **82**, 043435 (2010).
- [38] B. Chann, E. Babcock, L. W. Anderson, and T. G. Walker, *Phys. Rev. A* **66**, 033406 (2002).
- [39] W. De Heer, P. Milani, and A. Châtelain, *Z. Phys. D* **19**, 241 (1991).
- [40] Q. Sun, Q. Wang, and S. Wang, *Phys. Lett. A* **228**, 297 (1997).
- [41] N. Papanikolaou, N. Stefanou, R. Zeller, and P. H. Dederichs, *Phys. Rev. Lett.* **71**, 629 (1993).
- [42] W. A. de Heer, K. Selby, V. Kresin, J. Masui, M. Vollmer, A. Châtelain, and W. D. Knight, *Phys. Rev. Lett.* **59**, 1805 (1987).
- [43] N. D. Bhaskar, R. P. Frueholz, C. M. Klimcak, and R. A. Cook, *Phys. Rev. B* **36**, 4418 (1987).
- [44] T. Martin, *J. Chem. Phys.* **81**, 4426 (1984).
- [45] E. B. Alexandrov, M. V. Balabas, D. Budker, D. English, D. F. Kimball, C.-H. Li, and V. V. Yashchuk, *Phys. Rev. A* **66**, 042903 (2002).
- [46] A. Gozzini, F. Mango, J. Xu, G. Alzetta, F. Maccarrone, and R. Bernheim, *Nuovo Cimento D* **15**, 709 (1993).
- [47] A. Burchianti *et al.*, *Europhys. Lett.* **67**, 983 (2004).
- [48] Y. Li, E. Blaisten-Barojas, and D. A. Papaconstantopoulos, *Phys. Rev. B* **57**, 15519 (1998).
- [49] C. Witte, M. Kunth, F. Rossella, and L. Schröder, *J. Chem. Phys.* **140**, 084203 (2014).
- [50] N. Whiting, P. Nikolaou, N. A. Eschmann, B. M. Goodson, and M. J. Barlow, *J. Magn. Reson.* **208**, 298 (2011).
- [51] S. Mochizuki, K. Inozume, and R. Rupp, *J. Phys.: Condens. Matter* **11**, 6605 (1999).
- [52] A. B. A. Baranga, S. Appelt, M. V. Romalis, C. J. Erickson, A. R. Young, G. D. Cates, and W. Happer, *Phys. Rev. Lett.* **80**, 2801 (1998).
- [53] E. Babcock, B. Chann, T. G. Walker, W. C. Chen, and T. R. Gentile, *Phys. Rev. Lett.* **96**, 083003 (2006).
- [54] J. Singh *et al.*, [arXiv:1309.4004](https://arxiv.org/abs/1309.4004).
- [55] W. C. Chen, T. R. Gentile, Q. Ye, T. G. Walker, and E. Babcock, *J. Appl. Phys.* **116**, 014903 (2014).
- [56] W. C. Chen, T. R. Gentile, T. G. Walker, and E. Babcock, *Phys. Rev. A* **75**, 013416 (2007).
- [57] I. C. Ruset, Ph.D. thesis, University of New Hampshire, 2005.